An Antenna Based on Three Coupled Dipoles With Minimized E-Field for Ultra-High-Field MRI

Rustam Balafendiev, Georgiy Solomakha, Marc Dubois, Redha Abdeddaim, Stefan Enoch, Constantin R. Simovski, and Stanislav Glybovski

***Abstract*— In this work, we demonstrate an approach for local reduction of the electric field amplitude of the transmitted radio-frequency signal in ultrahigh-field magnetic resonance imaging (MRI). We excite a suitable combination of three coupled dipole hybrid resonances composing a single transmit antenna array element. Using numerical optimization, we designed a feeding network for three coupled dipoles placed over an electromagnetic phantom mimicking a human body. This network of discrete elements provides the appropriate amplitudes and phases of three dipole currents excited by a single input port. It allows controlling the electric field distribution in the vicinity of the antenna. Our goal was to obtain a minimum of the electric field at the given relatively small depth inside the phantom, where body implants are typically located while keeping a tolerable level of the magnetic field toward the phantom's center. We designed and manufactured a three-dipole antenna prototype optimized for MRI of the human body at 7 T (proton Larmor frequency of 298 MHz). The experimental validation showed a 40 dB reduction of the electric field amplitude at a depth of 4 cm compared to a conventional single-dipole antenna. The coupling network can be rearranged to target different depths. Therefore, a principle of electric field minimization at a controllable position inside the body has been shown, which may be useful for designing transmit MRI antennas with improved safety of implants.**

***Index Terms*— 7 T, antenna, dipole, magnetic resonance imaging (MRI), modes, specific absorption rate (SAR), ultrahigh field.**

I. Introduction

MAGNETIC resonance imaging (MRI) is a rapidly developing, noninvasive technology for early diagnostics of various diseases and clinical investigation of the human body. One of the current development trends is increasing the static field B_0 of superconductive magnets providing a higher signal-to-noise ratio and a higher resolution as well as better tissue contrast [1]. Ultrahigh-field MRI with a static magnetic field B_0 of 7 T has become available for clinical diagnostics of the human head and extremities. Ultrahigh-field MRI methods have been successfully employed for the investigation of the human brain [2] and early detection of cancer [3]. However, challenges remain in the development of RF hardware, and safety concerns slow the application of ultrahigh-field MRI to some clinical tasks, especially for body imaging.

Increasing B_0 leads to higher Larmor frequencies (for instance, 298 MHz at 7 T for proton nuclei), which are frequencies of excitation signals during the MRI scan. Due to the high permittivity of most human body tissues, the corresponding wavelength can be reduced to approximately 13 cm in the abdominal cavity [4]. Moreover, the conductivity of the tissues leads to a reduction of the penetration depth of the operational right-hand circularly polarized component of the magnetic field B_1^+ [expressed as $0.5(B_{1x}+iB_{1y})$ [5]] as well as a highly inhomogeneous amplitude and phase distribution of the same B_1^+ field across the body. This results in the hotspots transmitting electric field (as a spatial derivative of the magnetic field), leading to tissue heating. To achieve the needed signal-to-noise ratio for deeply located regions, higher levels of transmitted power are required than in conventional clinical MRI with 1.5/3 T field strength. For instance, an about twofold increase is required when going from 4 to 7 T [6]. This becomes one of the factors, which contribute to higher levels of specific absorption rate (SAR)—a measure of the rate at which the RF excitation of the human tissue is converted into the heating of the sample, calculated as $(1/V)\int(\sigma(\mathbf{r})|\mathbf{E}(\mathbf{r})|^2\backslash\rho(\mathbf{r}))dV$. SAR could be calculated at a point or averaged over the whole body volume or a small volume (typically 1 or 10 g of tissue).

Due to the wavelength reduction, B_1^+ amplitude and phase distributions become sample-specific, highly inhomogeneous, and thus hard to control using a single transmit antenna [7]. In contrast to high-field clinical MRI, where a volumetric "birdcage" resonator is used for relatively homogeneous excitation of the sample [8], the method of RF shimming is widely adopted in ultrahigh-field MRI [9], [10]. This method uses multiple antenna elements located near the body or head surface. These are typically driven with optimized phases to homogenize B_1^+ amplitude over the region of interest (ROI) for the available amount of transmit power. While optimization and MRI procedure have made impressive progress in recent years, RF shimming is not available in clinical applications due

Manuscript received 31 May 2021; revised 10 April 2022; accepted 21 May 2022. Date of publication 8 August 2022; date of current version 9 November 2022. This work was supported in part of experimental investigation by the Russian Science Foundation under Project 21-19-00707, in part of Matlab optimization by the FET-PROACT M-ONE (project grant #952106) and in part of numerical simulations by the European Union Horizon 2020 Research and Innovation Program under Grant 736937. *(Corresponding author: Rustam Balafendiev.)*

Rustam Balafendiev, Georgiy Solomakha, and Stanislav Glybovski are with the School of Physics and Engineering, ITMO University, 197101 St. Petersburg, Russia (e-mail: rustam.balafendiev@metalab.ifmo.ru).

Marc Dubois is with Multiwave Imaging, 13013 Marseille, France.

Redha Abdeddaim and Stefan Enoch are with Aix Marseille Univ, CNRS, Centrale Marseille, Institut Fresnel, Institut Marseille Imaging, 13013 Marseille, France.

Constantin R. Simovski is with the Department of Electronics and Nanoengineering, School of Electrical Engineering, Aalto University, 0007 Aalto, Finland.

Color versions of one or more figures in this article are available at https://doi.org/10.1109/TAP.2022.3195515.

Digital Object Identifier 10.1109/TAP.2022.3195515

to safety concerns. The elimination of the local SAR hotspots when using phased array antennas for body imaging at 7 T and above remains one of the most critical challenges in the future development of ultrahigh-field MRI.

Different types of antennas have been proposed as on-body (surface) array elements for ultrahigh-field body imaging such as loop coils [9], TEM transmission-line resonators [11], slots [12], dipoles [13]–[15], and leaky-wave antennas [16], as well as their combinations [17]. A way of combining the antenna array with excitation by a traveling-wave coil has also been proposed [18]. All these types of antennas differ by their resonant properties and amount of reactive electric fields localized near the antenna conductors, therefore, causing different SAR levels. A relationship between the quality factor and maximum local SAR created in the vicinity of the antenna was observed [16]. It is expected that less resonant antenna configurations can achieve lower SAR. Indeed, reducing SAR for the same B_1^+ is one of the most desirable results of transmit antenna optimization as it allows higher input power per array element while managing safety requirements on maximal local SAR.

Much effort has been made to reduce SAR created by surface antenna elements for ultrahigh-field body imaging. Despite loop coils traditionally being used in MRI as local antenna-array elements, their operation for body RF excitation at 7 T was found to be not optimal in terms of the ratio $B_1^+/\sqrt{\mathrm{SAR}_{max}}$ which is called the SAR efficiency. In the latter, B_1^+ is measured in the ROI (typically in the center of the body). At the same time, SAR_{max} is the maximum local SAR within the entire object. It was shown [13] that dipole antennas overcome loops in terms of SAR efficiency when used as elements of phased arrays for RF shimming, while loops may serve as additional receive-only elements [17]. First, introduced dipoles were mounted on bulky ceramic spacers to keep conservative electric fields mostly outside the object and to reduce SAR [14]. Later, several modifications of on-body dipole antennas were introduced to reduce electric fields and SAR. A bowtie antenna on a water-filled substrate was proposed to control the electric field for MR-controlled hyperthermia [15]. Ways of improving the coil's SAR efficiency by adding a shielding plate have been explored [19], [20]. The fractionated dipole with inductive bent strips and a thin low-permittivity spacer was shown in [21] to improve SAR efficiency in comparison to the first dipoles by optimizing the length and inductance of its bent conductors. In [22], the fractionated dipole was upgraded in terms of SAR by eliminating the high electric fields nearby the feeding point at the center using passive feeding. The idea of meandering for SAR reduction was further developed in the recently introduced "snake antenna" for body imaging at 10.5 T [23].

Another approach to SAR reduction looked into the homogeneous distribution of currents around the body compared to a previously proposed configuration of eight transmit dipoles. In this approach, each transmit antenna array element contained two parallel dipoles driven in-phase instead of one [24]. This dual-dipole antenna resulted in a 70% SAR reduction in comparison to the single fractionated dipole while having the same B_1^+ in the center of a sample. Here, the dipoles were modified to reduce SAR, thanks to lower local current amplitude and near electric field while maintaining high radiative fields dominant in the body's center. However, none of the previous designs provide the opportunity to cancel the electric field at a desirable point located relatively close to each antenna array element.

As well as lowering SAR, the reduction of the electric field can be used to protect the patient in cases when a conductive object is present near the surface of the patient's body [25]. For example, in cardiac imaging, such an object could be an artificial pacemaker [26], a lead [27], or a catheter [28], [29]. While for bulky implants, gradient heating can be much more significant [30], [31], for prolonged implants like leads and catheters, RF heating is the most considerable. For 7 T, it is mainly related to cardiac or prostate imaging. Other methods exist for mitigating the risk of heating of the implant and the surrounding tissues, such as modifying the implant's impedance to reduce the induced currents, for example, by adding coaxial chokes [32], [33]. However, such modifications of lead wires or cables can be detrimental to mechanical robustness and infeasible for patients with installed pacemakers. Another method of mitigating the electric field near the implant would be by using strategically located high-permittivity material pads [34]. However, this method is designed for lower static magnetic field strengths, where birdcage coils can still be utilized. Furthermore, since leads and catheters can take a number of trajectories through the body, a method of electric field reduction would need to be flexible enough to account for this. Using adaptive RF shimming has been demonstrated to be suitable to achieve this by minimizing the electric field created by the entire array, but not nearby the antenna elements [35], [36].

In this work, we propose and develop an antenna for ultrahigh-field MRI of the human body at 7 T that would allow us to manipulate the near-field distribution with an ability to minimize the electrical field level at the desired point or line near the surface while maintaining a high enough level of B_1^+ in the scanned region near the center of the body. Minimization of E-field is essential in the region right below the antenna, where for conventional antennas, a peak electric field is typically observed. Minimizing the E-field amplitude at a given depth will allow one to create a safe region under the surface and reduce the undesirable current in metallic implants situated in the same region. The proposed antenna containing three intrinsically coupled dipoles is demonstrated here on the bench and is intended for use in a transceive array for body imaging at 7 T.

II. Method for Electric Field Suppression

The excitation of a system of coupled resonators can be interpreted in terms of hybridized modes of the system. In our case, these modes can be likened to modes of current similar to those described in [37] and [38]. The field outside the system can be approximated by a linear combination of the modal fields, with coefficients depending on the excitation scheme and frequency. By controlling the excitation of the resonators, we can control their field distribution. In this work, we propose to minimize or suppress the electric field at a

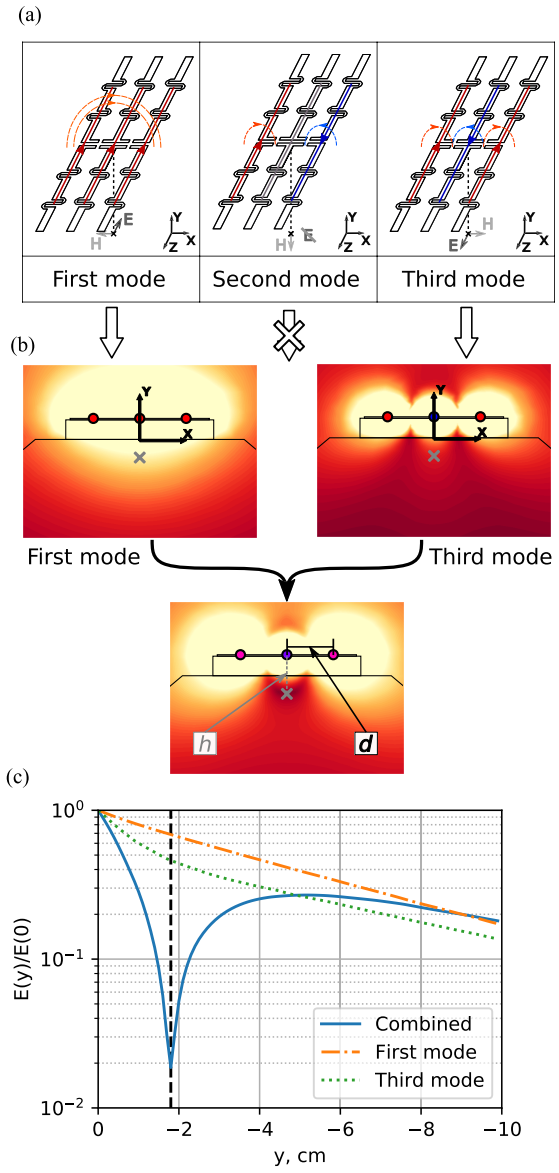

Fig. 1. Idea of the proposed method for minimizing electric field by combining two of three modes in a system of three coupled dipoles (symmetric case). (a) Hybridized modes of the structure. Currents are shown in red and blue, their respective magnetic fields in orange and light blue. (b) Electric fields of the first and third modes and a possible result of combining the two. Here, d is the distance between dipoles, and h is the distance from the central dipole feeding point to the minimum. (c) Normalized profiles along the y-axis of the electric fields shown above.

given depth inside the human body just below the antenna by combining the hybridized modes of three coupled dipoles. To show the principle, we consider three fractionated dipoles placed in parallel to each other as shown in Fig. 1(a). In the structure of three electrically coupled dipole antennas, three hybridized modes exist. First is the "dipole" mode, in which the current along all three dipoles flows in phase, essentially forming a single wide strip of current radiating similar to a thick dipole antenna, creating lower reactive fields. The second is the "loop-like" mode, where the two-side dipoles have their currents facing opposite directions, while the middle one does not contribute at all. The field related to this mode can be attributed to a vertical magnetic dipole formed by two opposite currents with a noticeable distance between them. However, such a system of currents also has an off-diagonal quadrupole term that implies the difference of the modal electromagnetic field from the field of a magnetic dipole beyond the H-plane of the system (xy-plane). In the H-plane, and, in particular, on the y-axis, the fields of magnetic dipole and off-diagonal quadrupole are nondistinguishable from one another. The third is a "figure-8-like" mode, with the currents on the side dipoles being antiparallel to the middle one. The field effect of this mode is similar to a magnetic quadrupole combined with an electric dipole to account for the possible difference between the current amplitudes of the center dipole and the side ones. When considering the field right below the middle dipole (in the near- and intermediate-field regions on the y-axis), the first and third modes produce horizontal (X-directed) components of the magnetic field, while the second mode produces a vertical (Y-directed) magnetic field component. At the same time, the first and third modes produce an electric field in the parallel direction along the z-axis [see Fig. 1(a)]. By finding the correct excitations, one can have electric fields of the first and third modes cancel each other due to destructive interference at a given position along the y-axis [39]. It can be shown that when the excitation is done with a number of dipoles aligned along Z canceling the Z-component of the electric field is enough for a significant reduction of SAR since even at their respective maximums near the ends of the dipoles the contribution of X-and Y-components to SAR is about four times less than that of the Z-component at the center. It can be said that the Z-component is what primarily decides the position and magnitude of the maximum of SAR and minimizing it is equivalent to minimizing SAR_{max}.

Let us assume that the dipoles are all aligned, and two of them are placed symmetrically at a distance d from the middle one, which is positioned on the z-axis. Thanks to the common direction of the electric field and the exact even symmetry with respect to the x-axis, a proper combination of the first and third modes minimizes the total electric field at a point along the y-axis. The further the point, the more significant is the required magnitude of the third mode in comparison to the first one. When the antisymmetric second mode is added, the point at which the electric field can be canceled can be shifted off the yz-plane. In this work, for simplicity, we limit ourselves by placing the target point for electric field cancellation along the y-axis. Both the position of such a point and the above-described mode interference are shown in Fig. 1(b).

With the increase of the mode order, the field strength decreases more rapidly with a distance from the antenna plane. As illustrated in Fig. 1(c), in our case, the field of the third mode decays more rapidly than that of the first one. Nevertheless, when excited with sufficient amplitude, the third mode becomes capable of canceling the electric field of the first mode even at a relatively large distance in the y-direction. In the presence of a conducting object mimicking a human pelvis (called a phantom), this combination principle is still valid: one can combine the first and third modes (and optionally the second one in the asymmetric case) with particular

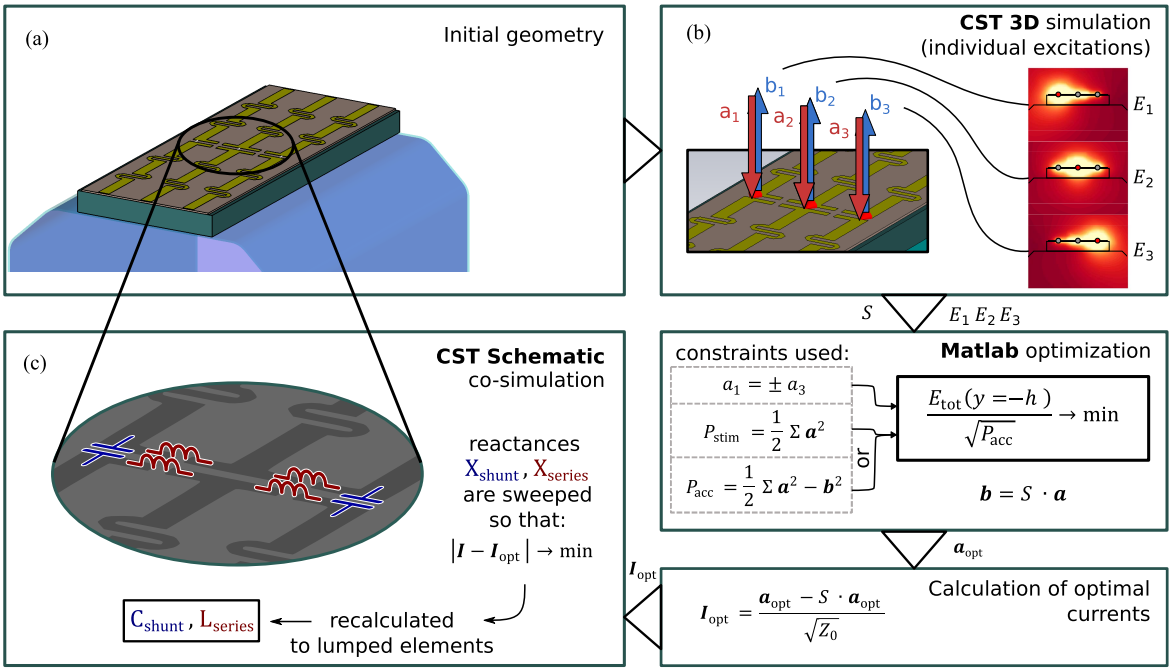

Fig. 2. Block diagram of the optimization algorithm used for determination of lumped elements for the minimized electric field at a given depth in the phantom. (a) Antenna geometry in CST MWS. (b) Representation of the method of obtaining electric fields of individual ports and their S-matrix. (c) Recalculated reactances as they are placed on the antenna.

amplitudes and phases to minimize (or maximize) the field in the region of the object located below the center of the antenna while not diminishing the magnetic field at larger depths to some extent.

A. Proposed Antenna Design

The proposed antenna consists of three identical parallel dipoles [see Fig. 2(a)] connected by reactive circuit elements and fed at one port in the middle of the central dipole. By loading the side dipoles by shunt capacitance C_{shunt} and connecting the dipoles using series inductances L_{series} [see Fig. 2(c)], it is possible to excite the required linear combination of the first and third modes using just one port. It is important to use one port per antenna since the number of transmit channels used in the RF shimming approach in state-of-the-art MR systems is limited. The proposed antenna comprising three dipoles and driven with one port is considered as a single element of a transmitting array for body imaging at 7 T. The choice of reactive impedances of the lumped elements then sets the phase shift and amplitude of the side dipole currents relative to the central dipole.

The practical realization of the triple-dipole antenna designed for 298 MHz (Larmor frequency of 7 T proton MR imaging) consists of three parallel fractionated 30 cm long dipoles printed on top of a 1.5 mm thick FR-4 substrate with the dimensions of 12 × 30.8 cm^2 and relative permittivity of 4.3 (each one is similar to the dipole proposed in [14]). The substrate was placed over a 2 cm thick polycarbonate spacer to limit SAR levels as was previously done for single on-body dipole antennas [21]. The dipole's axes are positioned at a distance $d = 4$ cm away from each other. The dipoles

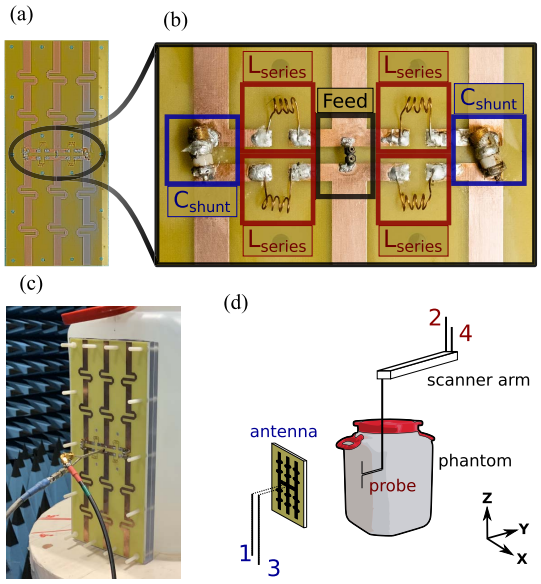

Fig. 3. Configuration used for on-bench measurements. (a) Three dipoles, printed on a PCB substrate and connected by a coupling network. (b) Close-up of the coupling network. (c) Photograph of the manufactured triple-dipole antenna on a polycarbonate spacer connected to VNA and attached to a phantom. A probe is connected to the arm of the near-field scanner placed inside the phantom. (d) Schematic representation of the same setup.

themselves are 1 cm wide copper strips. The geometry of each dipole is the same as in [21], the only difference being an addition of half-centimeter-long stubs in-between the dipoles' arms for embedding coupling circuit elements for proper excitation of modes [see Fig. 3(a)]. Hand-wound inductor coils

and nonmagnetic adjustable air trimmer capacitors with the capacitance range of 0.8–10 pF were used for setting the necessary reactances of the coupling network [see Fig. 3(b)].

B. Simulation and Optimization

First, electromagnetic fields in a pelvis-shaped homogeneous phantom were calculated using CST Microwave Studio 2018. For simplicity, only z-component of E-field was taken into account since according to our simulation, for a single dipole, only E_z defines the local maximum of SAR. E_z in the phantom was exported to the MATLAB R2017b software for optimization of a triple dipole antenna. The phantom had the averaged dielectric properties of human body tissues at 7 T [13] ($\varepsilon = 34$ and $\sigma = 0.45$ S/m). Each of the three dipoles without circuit elements individually fed via lumped 50 Ω ports [shown as red cones in Fig.2(b)]. For each port excitation, the other two ports were loaded by 50 Ω loads that allowed to calculate and export the S-matrix as well. Then, in the second step, obtained electromagnetic field distributions can be combined to find excitation phases and amplitudes that would minimize the electric field magnitude at a given point. The optimization was done with the MATLAB R2017b optimization toolbox. As a constraint, excitation amplitudes of the two side dipoles were set to be equal to ensure only the symmetrical modes were excited. The vector of optimized excitations **a** was used in conjunction with the exported 3×3 matrix of S-parameters to find the **b** vector of the reflected wave complex magnitudes. This allows us to calculate forward or accepted power (P_{stim} and P_{acc}, respectively) and use either of the two as constraints in order to compare different cases quantitatively. When finding the optimal current magnitudes and phases, we kept the accepted power constant and ensured to minimize the level of E-field. In the third step, these **a** and **b** were used with input impedance $Z_0 = 50$ Ω to find the vector of currents **I** at the input of each dipole as $\mathbf{I} = (\mathbf{a} - \mathbf{b})/\sqrt{Z_0}$. The goal was to obtain the minimum of the electric field at the given depth inside the phantom normalized by the square root of accepted power. While B_1^+ could be separately maximized at the same time, it will likely compromise the convergence of the optimization and slow down the optimization procedure. Finally, in the fourth step, the values of the reactive elements were found by a 2-D sweep across series (X_{series}) and shunt (X_{shunt}) reactances, while using only one port in the middle. The target function in choosing the reactances was the distance of the vector of resulting complex-valued currents to the optimized vector obtained at the first optimization step. This strategy, graphically represented as a block diagram in Fig. 2, helps to avoid recalculating full 3-D simulations for every reactance value tested and requires a few minutes of computation on a regular PC (Intel i5 7600 CPU, 32 GB RAM).

As a result, by interconnecting the dipoles with the determined lumped reactive elements, the optimized currents were found to minimize the electric field level at a given depth using only one fed port. In this way, one obtains an antenna element that intrinsically creates a minimum of the electric field at a desirable depth, for example, in the implant's assumed position in a human body.

The reactive impedance values that were found in the previous step are then included in the numerical simulation of the proposed antenna as lumped elements. The reactance values were then swept once again in a 3-D simulation model of CST to accommodate any inconsistencies introduced by using lumped elements in schematic cosimulation and improving the achieved E-field reduction. The simulation aimed to confirm the existence of the supposed minimum of the electric field as well as to investigate the antenna's performance regarding B_1^+ and SAR_{max}.

C. Near-Field Measurements and Performance Evaluation

In order to validate the numerically calculated result, the electric and magnetic fields in the phantom were measured on the bench using asymmetric dipole and loop probes. The electric probe was aligned along Z, while the loop probe was placed in parallel to the zy-plane. The phantom was filled with a mixture of distilled water and ethanol (with a ratio of about 1–5) with NaCl added and had the same dielectric properties as the phantom in the simulation. The complex permittivity of the solution was measured using the SPEAG DAK-12 precision dielectric measurement system and Agilent E8362C vector network analyzer (VNA). The phantom used in the measurements was made using a 30 L plastic container with about $26 \times 26 \times 43$ cm size. Because the cross section of the canister had a shape of a chamfered and slightly rounded square, only about 20 cm of the side was a usable flat surface. The container had a 21.5 cm wide circular neck.

The photograph of the fabricated antenna printed on the FR4 substrate is shown in Fig. 3(c). The experimental setup is presented in Fig. 3(d). It consists of the antenna, the phantom, a near-field scanner, and a probe connected to the scanner. The electric probe was then used to scan through the phantom to obtain a 3-D pointmap of the Z-component of the electric field, while the magnetic loop probed the X-component of the magnetic field. Both the probe and the investigated antenna were connected to the four-port R&S ZVB20 VNA using paired coaxial cables driven in the differential mode to avoid the cable effect (logical port mode). The cable effect appears due to the improper connection of an asymmetric-type transmission line to a symmetric antenna causing the even mode of current flowing in the transmission line and distorting the field pattern. Ports 1 and 3 were combined as a logical port of the dipole, while ports 2 and 4 were combined as the logical port connected to the probe. The electric field was measured indirectly via the differential-mode transmission coefficient S_{dd12} between the antenna port and the probe and normalization to accepted power calculated through the differential-mode reflection coefficient at the dipole port S_{dd11} as $S_{\text{dd12}}/\sqrt{P_{\text{acc}}} = S_{\text{dd12}}/\sqrt{(1 - |S_{\text{dd11}}|^2)}$. The resulting 4×4 S-parameter matrix of four physical ports was then used to reconstruct 2×2 S-parameters of the balanced two-port network as $S_{\text{dd12}} = (S_{12} - S_{14})/2 - (S_{32} - S_{34})/2$, $S_{\text{dd11}} = (S_{11} - S_{33})/2 - (S_{22} - S_{44})/2$.

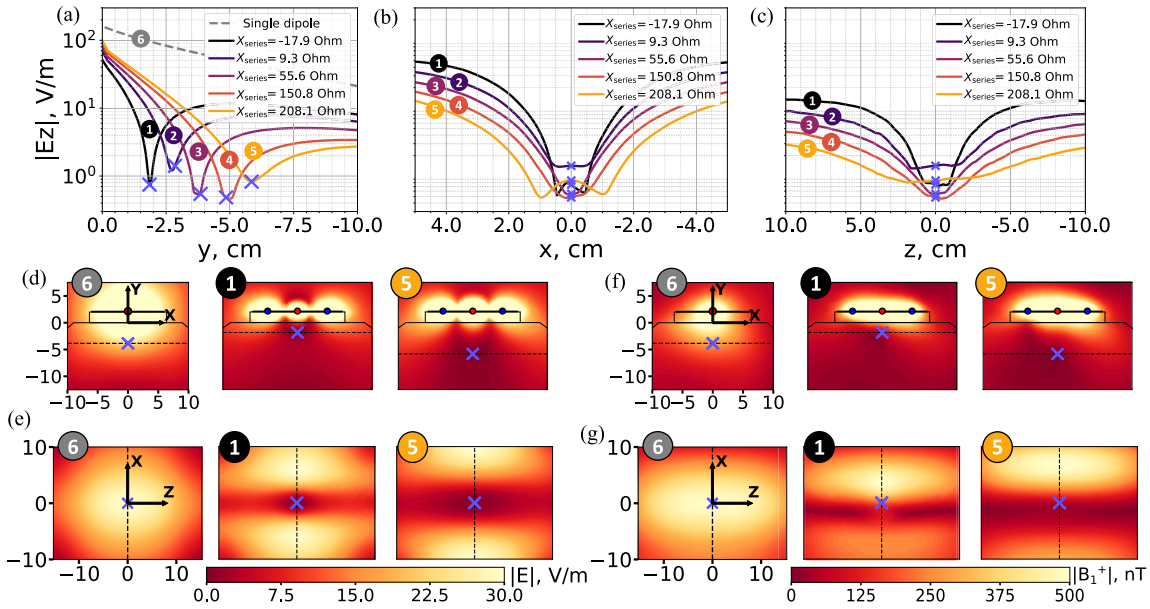

Fig. 4. Numerically calculated electric field profiles for different optimization depths (at the accepted power of 0.5 W). Expected positions of the field minimums are marked with blue cross markers. The different curves correspond to different series reactances X_{series}. (a) Depth profiles along the y-axis (below the middle of the central dipole). (b) Field distribution along the transverse X-coordinate at the optimized depth. (c) Same as (b), but along the longitudinal Z-coordinate. (d) 2-D E-field distributions, xy-plane. (e) 2-D E-field distributions, xz-plane, at the optimal depth. (f) 2-D B_1^+-field distributions, xy-plane. (g) 2-D B_1^+-field distributions, xz-plane, at the optimal depth.

TABLE I

RESULTS OF THE SIMULATION. DECREASE IN ELECTRIC FIELD STRENGTH IS MEASURED RELATIVE TO A SINGLE DIPOLE DRIVEN WITH THE SAME ACCEPTED POWER

Target depth, h	4 cm	5 cm	6 cm	7 cm	8 cm
X_{series}, Ohm	-17,9	9,3	55,6	150,8	208,1
X_{shunt}, Ohm	-48,2	-53,7	-62,1	-68,6	-68,6
Relative depth error	1.08%	4.21%	0.78%	3.51%	0.17%
E-field reduction, dB	-42,2	-34,7	-41,3	-40,7	-34,4

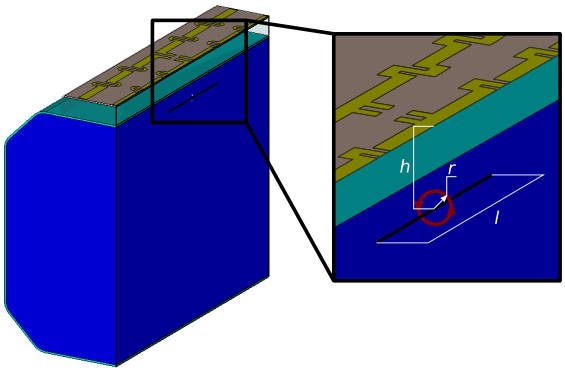

Fig. 5. Model of a metallic lead inside the phantom. The red circle marks the integration path used to calculate the current.

III. NUMERICAL RESULTS OF ELECTRIC FIELD MINIMIZATION

The reactance values found after the optimization are presented in Table I. In the case of decreasing depth, the series reactance gradually decreases before passing over zero and becoming negative as the optimization point approaches the surface. This negative reactance can then be recalculated into corresponding capacitance. The shunt reactance stayed negative across the entire range of investigated depths. Overall, when recalculated from the reactances, the values of the inductances and capacitances typically stayed below 120 nH and 20 pF, respectively. Most of the values found via MATLAB gave an immediate result, except for the ones with the absolute values of their reactive impedances closest to zero. This can be explained by the parasitic reactances of the geometry playing a comparatively more significant role. As such, some values (namely, for depths h of 4 and 5 cm) were adjusted with another sweep after running a CST simulation in order to have their minimums be closer to the target coordinates. The numerically calculated field profiles for reactances optimized for different depths are presented in Fig. 4 and compared to the single dipole case. By setting various depths h as targets for optimization, we have shown that the electric field minimum can be obtained at any depth from 1 to 6 cm [see Fig. 4(a)]. The difference between the expected minimization depth and realized depth in full-wave simulation is given in Table I. As can be seen from Fig. 4(a) and (b), for most depths, the region of lowered field is about twice as wide in the z-direction as it is in the x-direction. In fact, for the z-direction, the field decrease is not confined to the aforementioned region, with about a fivefold lower field under the middle dipole in comparison to a single dipole for the entirety of its length [see Fig. 4(e)]. This is beneficial since the implants that offer the most cause for concern of heating due to the E-field are prolonged and typically oriented along the z-axis. Fig. 4(d) and (e) shows the way the area of a significantly lower field gradually becomes less and less confined as the

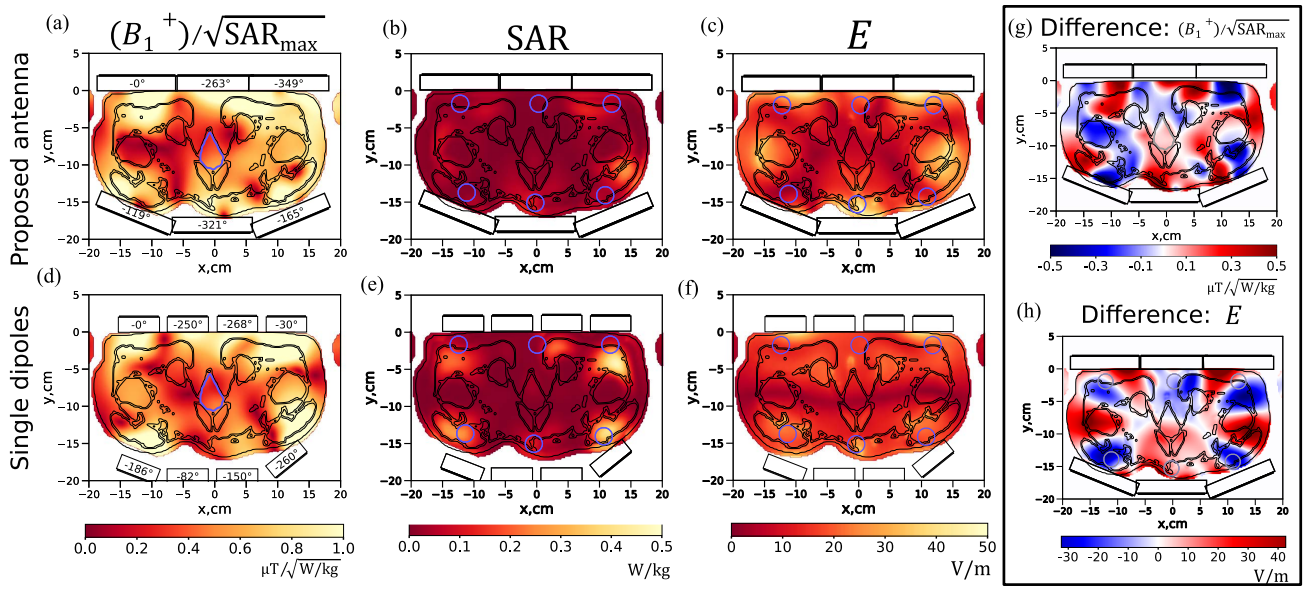

Fig. 6. Results of numerical simulations of antenna arrays placed on a voxel model of the human body. SAR efficiency, as well as SAR and electric field distributions. (a)–(c) Array of the proposed type. (d)–(f) Array of single fractionated dipoles. (g) and (h) Difference between the two. ROIs [the center for (a) and (d) and target points for E-field minimization for the rest] are marked with blue contours. SAR and E-field distributions in both cases are normalized to respective forward power or to the square root of forward power.

TABLE II
DECREASE IN CURRENT AMPLITUDE ON THE LEAD

Target depth, h	4 cm	5 cm	6 cm	7 cm	8 cm
Current for 1 dipole, mA	40,4	32,9	27,1	22,2	18,2
Current for 3 dipoles, mA	2,3	1,5	1,1	0,7	0,5
Current reduction, dB	-24,8	-26,9	-28,1	-29,5	-31,5

depth increases. This demonstrates the problem in creating such a minimum at a considerable distance away from the antenna, where the near-field contribution will be significantly lower. Fig. 4(f) and (g) shows that this also applies to the magnetic field with the region of the lowered field being wider for deeper minima.

A circular metal wire with a diameter of 1 mm and length $l = 10$ cm modeling an implanted lead was then placed inside the phantom at the optimized depth h to verify that the minimization of the electric field corresponds to the lowering of the current induced in a prolonged implant (see Fig. 5). The current amplitude was calculated by integrating the magnetic field along the circular contour with radius $r = 3$ mm around the wire. The results are presented in Table II. A current reduction of about 20 times was observed. The stronger reduction of current at greater depths confirms the elongated shape of the field minimum being beneficial.

Another group of simulations was aimed at gauging the performance of the proposed antenna when used as an element of a six-channel array, mainly by comparing SAR efficiency, with that given by an array of eight single dipole antennas. For both antenna types, the procedure of phase RF shimming was applied. In other words, each antenna of the array was fed with an individually selected initial phase [shown in Fig. 6(a) and (d)] to interfere in-phase and maximize B_1^+ magnitude at one point (at the center of the body model). The Gustav voxel model from the CST Studio voxel model family was used to estimate the SAR efficiency in the center of the body model, as well as SAR and E-field distributions. The results (normalized to forward power) are compiled in Fig. 6. The decoupling performance of the two arrays after matching is demonstrated in Fig. 7. The reactances of the lumped elements used were previously optimized on a phantom for creating a minimum of an electric field at a depth of 2 cm. When estimated at the center (for the B_1^+ field averaged in the region of the prostate), the proposed configuration resulted in about 29% better performance in terms of SAR efficiency [see Fig. 6(a) and (d)] and 6% in terms of transmit efficiency (see Table III). Transmit efficiency here is defined as the ratio of the averaged B_1^+ field to the square root of the transmitted power. As such, it could be stated that when compared to the single dipoles, the proposed coil does not have worse imaging capabilities in the ROI. For comparison, eight-channel dual-mode dipole array [24] were simulated. This array could provide higher SAR efficiency in comparison to the proposed array. Still, it could not allow E-field manipulation in the desired region. This depth of 2 cm corresponds to electric field minimization in a specific location of a prolongated metal orthopedic implant, for example, a femur or pelvis implant. The point with the depth of 9 cm, in which B_1^+ field and efficiency are found, corresponds to a position of the human prostate, one of the important ROIs in ultrahigh-field MRI. Due to the dielectric properties in the human body not being homogeneous because of variation between tissues and to some part due to the interference between the array elements, the minimization of the field could not be achieved to the same extent as in the phantom for one antenna only. Nevertheless, the impact of the mode interaction can be seen in the disappearance of the two SAR maximums on the right side of the model [see Fig. 6(e) and (b)] and the lower electric

TABLE III
COMPARISON BETWEEN THE TRIPLE, SINGLE, AND DUAL-MODE DIPOLE ARRAYS

	Triple	Single	Diff.	Dual
SAR efficiency, $\mu T/\sqrt{W/kg}$	0.221	0.171	29.1%	0.383
Transmit efficiency, $\mu T/\sqrt{W}$	0.134	0.126	6%	0.331
Max local SAR, W/kg	0.29	0.47	38.1%	0.235
Mean $\|E\|$ at target points, V/m	7.6	32	76.1%	20.3
$\|E\|$ at bottom left point, V/m	0.8	28.5	97.2%	16

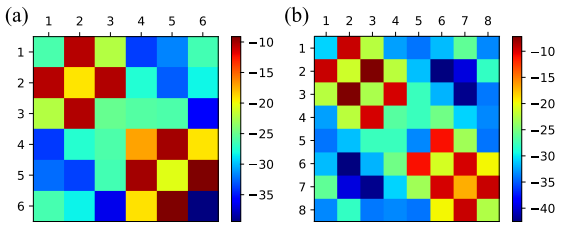

Fig. 7. S-matrices of antenna arrays after matching. (a) Six proposed antennas. (b) Eight single dipoles. The antennas are numbered clockwise, starting with the leftmost one at the top.

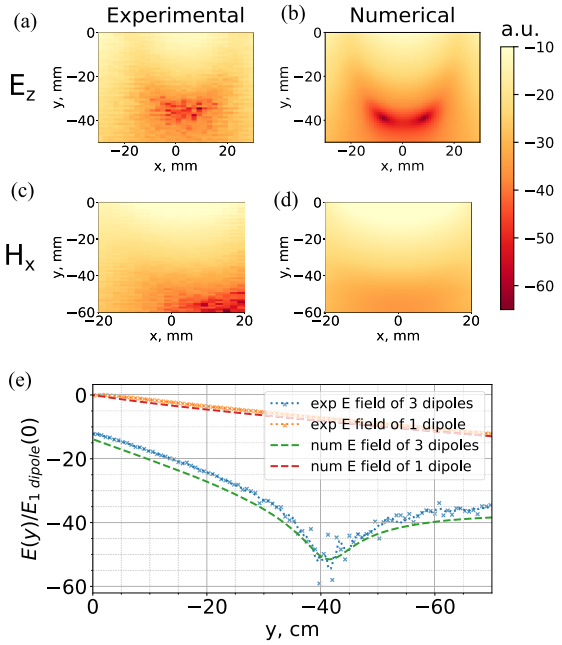

Fig. 8. Electric and magnetic field distributions of the proposed antenna (Z- and X-components, respectively) in numerical simulation and experiment normalized to the respective single-dipole field. (a)–(d) Comparison between 2-D field distributions. (e) Depth profiles of the electric field.

field beneath the antenna centers compared to the case of the single dipoles [with the best case of the lower-left antenna having the field more than 20 times lower at the estimated point; Fig. 6(c) and (f)]. Generally, most of the six elements of the proposed type clearly demonstrate the required local minima of the electric field, as can be seen in Fig. 6(c) and (f). Therefore, in comparison to an array of single dipoles, the proposed elements provided significant electric field reduction nearby each array element position while showing better SAR efficiency for the center of the body model.

IV. On-Bench Measurement of Electric and Magnetic Field Distributions

To investigate the effect of the optimal combination of the exciting eigenmodes on the field created by the proposed antenna, its electric and magnetic field components inside a phantom were numerically calculated and measured for the optimization depth of 4 cm. The lumped elements were manually tuned with their initial values taken from the simulation. Results presented were obtained with $L_{series} \approx 47$ nH, $C_{shunt} \approx 8$ pF as opposed to 33 nH and 6.2 pF in the simulations. The 2-D field distributions that were measured are presented in Fig. 8(a) and (c). The corresponding simulated field distributions are also presented in Fig. 8(b) and (d) for comparison. A single dipole with the same geometry as described above was numerically and experimentally investigated as a reference. The field distribution along the y-axis and a 2-D map for the triple-dipole antenna and the reference dipole were normalized by the field values of the single dipole taken at the surface ($y = 0$). Consequently, as can be seen in Fig. 8(e), the simulation and measurement results agree very well not only in terms of the electric field minimum shape, but also in terms of magnitude. In both simulations and measurements, similar U-shaped regions with noticeably suppressed electric fields arise. At these minimum points, electric field reduction to about -70 dB can be observed for both cases. However, the experimental case proves to be somewhat asymmetrical, with only one sharp minimum present on the right side. That said, the fact that either field has its minimums off-center can be explained by not exact equivalence between the values of the variable parallel capacitance connected in two sides dipole set in the experiment.

The relative magnetic field distributions of three dipoles to a single dipole are presented in Fig. 8(c) and (d) for simulations and measurements, correspondingly. While the minimum of the H-field in the experiment got shifted to the right (possibly due to unequally tuned capacitors on the left and right dipoles), along the center line, it still maintains a very similar profile to the numerical result—declining steadily up until about 6 cm, where it seemingly starts slowly climbing back up after reaching about the level of about -40 dB.

As was discussed earlier, since we are working with near fields, magnitudes of E- and H-field are not as closely tied to each other as they would be in the far-field, which results in the minimum of the H-field being approximately 2 cm deeper and not as prominent as the E-field one.

V. Conclusion

In this work, we proposed a method to manipulate near electric field distribution via combining the hybridized modes in an antenna composed of three coupled dipoles. To show the principle, we designed an on-body phased array comprising six proposed antenna elements operating at the Larmor frequency of protons in 7 T MRI. The three dipoles of the antenna are connected using lumped reactive circuit elements, optimized for a drastic reduction of the electric field at a certain point in

the scanned object. The shown principle can help increase the RF safety of metal and electronic implants during MRI scans. It is also potentially applicable to other problems where sharp field extrema can benefit, such as hyperthermic treatment. The numerical simulations have shown the predicted local minimum to be present at a given depth in a homogeneous phantom and to remain in a realistic human body model. An experimental investigation supported the existence of such a minimum in the phantom.

REFERENCES

[1] M. E. Ladd *et al.*, "Pros and cons of ultra-high-field MRI/MRS for human application," *Prog. Nucl. Magn. Reson. Spectrosc.*, vol. 109, pp. 1–50, Dec. 2018.

[2] A. Abosch, E. Yacoub, K. Ugurbil, and N. Harel, "An assessment of current brain targets for deep brain stimulation surgery with susceptibility-weighted imaging at 7 Tesla," *Neurosurgery*, vol. 67, no. 6, pp. 1745–1756, 2010.

[3] S. Gruber *et al.*, "Dynamic contrast-enhanced magnetic resonance imaging of breast tumors at 3 and 7 T: A comparison," *Invest. Radiol.*, vol. 49, no. 5, pp. 354–362, 2014.

[4] A. G. Webb and C. M. Collins, "Parallel transmit and receive technology in high-field magnetic resonance neuroimaging," *Int. J. Imag. Syst. Technol.*, vol. 20, no. 1, pp. 2–13, Feb. 2010.

[5] D. I. Hoult, "The principle of reciprocity in signal strength calculations—A mathematical guide," *Concepts Magn. Reson.*, vol. 12, no. 4, pp. 173–187, 2000.

[6] J. T. Vaughan *et al.*, "7T vs. 4T: RF power, homogeneity, and signal-to-noise comparison in head images," *Magn. Reson. Med.*, vol. 46, no. 1, pp. 24–30, Jul. 2001.

[7] J. T. Vaughan *et al.*, "Whole-body imaging at 7T: Preliminary results," *Magn. Reson. Med.*, vol. 61, no. 1, pp. 244–248, Jan. 2009.

[8] C. E. Hayes, W. A. Edelstein, J. F. Schenck, O. M. Mueller, and M. Eash, "An efficient, highly homogeneous radiofrequency coil for whole-body NMR imaging at 1.5 T," *J. Magn. Reson.*, vol. 63, no. 3, pp. 622–628, Jul. 1985.

[9] Y. Zhu, "Parallel excitation with an array of transmit coils," *Magn. Reson. Med.*, vol. 51, no. 4, pp. 775–784, 2004.

[10] P. Bluem, P.-F. Van De Moortele, G. Adriany, and Z. Popović, "Excitation and RF field control of a human-size 10.5-T MRI system," *IEEE Trans. Microw. Theory Techn.*, vol. 67, no. 3, pp. 1184–1196, Mar. 2019.

[11] C. J. Snyder *et al.*, "Comparison between eight- and sixteen-channel TEM transceive arrays for body imaging at 7 T," *Magn. Reson. Med.*, vol. 67, no. 4, pp. 954–964, Apr. 2012.

[12] L. Alon *et al.*, "Transverse slot antennas for high field MRI," *Magn. Reson. Med.*, vol. 80, no. 3, pp. 1233–1242, Sep. 2018.

[13] A. J. E. Raaijmakers, P. R. Luijten, and C. A. T. van den Berg, "Dipole antennas for ultrahigh-field body imaging: A comparison with loop coils," *NMR Biomed.*, vol. 29, no. 9, pp. 1122–1130, 2016.

[14] A. J. E. Raaijmakers *et al.*, "Design of a radiative surface coil array element at 7 T: The single-side adapted dipole antenna," *Magn. Reson. Med.*, vol. 66, no. 5, pp. 1488–1497, Nov. 2011.

[15] L. Winter *et al.*, "Design and evaluation of a hybrid radiofrequency applicator for magnetic resonance imaging and RF induced hyperthermia: Electromagnetic field simulations up to 14.0 Tesla and proof-of-concept at 7.0 Tesla," *PLoS ONE*, vol. 8, no. 4, Apr. 2013, Art. no. e61661.

[16] G. Solomakha *et al.*, "A self-matched leaky-wave antenna for ultrahigh-field magnetic resonance imaging with low specific absorption rate," *Nature Commun.*, vol. 12, no. 1, p. 455, Dec. 2021.

[17] M. A. Ertürk, A. J. E. Raaijmakers, G. Adriany, K. Uğurbil, and G. J. Metzger, "A 16-channel combined loop-dipole transceiver array for 7 Tesla body MRI," *Magn. Reson. Med.*, vol. 77, no. 2, pp. 884–894, Feb. 2017.

[18] I. A. Elabyad, T. Herrmann, C. Bruns, J. Bernarding, and D. Erni, "RF shimming and improved SAR safety for MRI at 7 T with combined eight-element stepped impedance resonators and traveling-wave antenna," *IEEE Trans. Microw. Theory Techn.*, vol. 66, no. 1, pp. 540–555, Jan. 2018.

[19] Z. Chen, K. Solbach, D. Erni, and A. Rennings, "RF coil element with longitudinal and transversal two-peak field distribution for low SAR 7-Tesla magnetic resonance imaging," in *IEEE MTT-S Int. Microw. Symp. Dig.*, Jun. 2013, pp. 1–4.

[20] Z. Chen, K. Solbach, D. Erni, and A. Rennings, "Electromagnetic field analysis of a dipole coil element with surface impedance characterized shielding plate for 7-T MRI," *IEEE Trans. Microw. Theory Techn.*, vol. 64, no. 3, pp. 972–981, Mar. 2016.

[21] A. J. Raaijmakers *et al.*, "The fractionated dipole antenna: A new antenna for body imaging at 7 Tesla," *Magn. Reson. Med.*, vol. 75, no. 3, pp. 1366–1374, 2016.

[22] I. Zivkovic, C. A. Castro, and A. Webb, "Design and characterization of an eight-element passively fed meander-dipole array with improved specific absorption rate efficiency for 7 T body imaging," *NMR Biomed.*, vol. 32, no. 8, p. e4106, Aug. 2019.

[23] B. Steensma *et al.*, "Introduction of the snake antenna array: Geometry optimization of a sinusoidal dipole antenna for 10.5T body imaging with lower peak SAR," *Magn. Reson. Med.*, vol. 84, no. 5, pp. 2885–2896, Nov. 2020.

[24] G. Solomakha *et al.*, "The dual-mode dipole: A new array element for 7T body imaging with reduced SAR," *Magn. Reson. Med.*, vol. 81, no. 2, pp. 1459–1469, Feb. 2019.

[25] Y. Eryaman, B. Akin, and E. Atalar, "Reduction of implant RF heating through modification of transmit coil electric field," *Magn. Reson. Med.*, vol. 65, no. 5, pp. 1305–1313, 2011.

[26] A. M. Ferreira, F. Costa, H. Marques, N. Cardim, A. Tralhao, and P. Adragao, "MRI-conditional pacemakers: Current perspectives," *Med. Devices: Evidence Res.*, vol. 7, no. 1, p. 115, May 2014.

[27] K. M. Walsh, A. G. Machado, and A. A. Krishnaney, "Spinal cord stimulation: A review of the safety literature and proposal for perioperative evaluation and management," *Spine J.*, vol. 15, no. 8, pp. 1864–1869, Aug. 2015.

[28] M. K. Konings, L. W. Bartels, H. F. M. Smits, and C. J. G. Bakker, "Heating around intravascular guidewires by resonating RF waves," *J. Magn. Reson. Imag.*, vol. 12, no. 1, pp. 79–85, 2000.

[29] W. R. Nitz, A. Oppelt, W. Renz, C. Manke, M. Lenhart, and J. Link, "On the heating of linear conductive structures as guide wires and catheters in interventional MRI," *J. Magn. Reson. Imag.*, vol. 13, no. 1, pp. 105–114, 2001.

[30] L. Zilberti, A. Arduino, O. Bottauscio, and M. Chiampi, "The underestimated role of gradient coils in MRI safety," *Magn. Reson. Med.*, vol. 77, no. 1, pp. 13–15, Jan. 2017.

[31] R. Brühl, A. Ihlenfeld, and B. Ittermann, "Gradient heating of bulk metallic implants can be a safety concern in MRI," *Magn. Reson. Med.*, vol. 77, no. 5, pp. 1739–1740, May 2017.

[32] O. Ferhanoglu, Y. Eryaman, and E. Atalar, "MRI compatible pacemaker leads," *Proc. Int. Soc. Mag. Reson. Med.*, vol. 13, p. 963, Jan. 2005.

[33] M. E. Ladd and H. H. Quick, "Reduction of resonant RF heating in intravascular catheters using coaxial chokes," *Magn. Reson. Med.*, vol. 43, no. 4, pp. 615–619, 2000.

[34] Z. Yu, X. Xin, and C. M. Collins, "Potential for high-permittivity materials to reduce local SAR at a pacemaker lead tip during MRI of the head with a body transmit coil at 3 T," *Magn. Reson. Med.*, vol. 78, no. 1, pp. 383–386, 2017.

[35] C. E. McElcheran *et al.*, "Numerical simulations of realistic lead trajectories and an experimental verification support the efficacy of parallel radiofrequency transmission to reduce heating of deep brain stimulation implants during MRI," *Sci. Rep.*, vol. 9, no. 1, p. 2124, Dec. 2019.

[36] B. Guerin, L. M. Angelone, D. Dougherty, and L. L. Wald, "Parallel transmission to reduce absorbed power around deep brain stimulation devices in MRI: Impact of number and arrangement of transmit channels," *Magn. Reson. Med.*, vol. 83, no. 1, pp. 299–311, Jan. 2020.

[37] P. Grahn, A. Shevchenko, and M. Kaivola, "Electromagnetic multipole theory for optical nanomaterials," *New J. Phys.*, vol. 14, no. 9, Sep. 2012, Art. no. 093033.

[38] A. Shevchenko, V. Vashistha, M. Nyman, and M. Kaivola, "Electromagnetic anapoles of a Cartesian expansion of localized electric currents," *Phys. Rev. Res.*, vol. 2, no. 4, pp. 1–5, Dec. 2020.

[39] R. Balafendiev, G. Solomakha, M. Dubois, R. Abdeddaim, C. Simovski, and S. Glybovski, "A method for E-field reduction using a surface coil based on three coupled dipoles," in *Proc. AIP Conf.*, vol. 2300, Dec. 2020, Art. no. 020006.

Rustam Balafendiev received the M.Sc. degree in radiophysics from the School of Physics and Engineering, ITMO University, Saint Petersburg, Russia, in 2021, where he is currently pursuing the Ph.D. degree.

His current research interests include surface coils for ultrahigh-field magnetic resonance imaging (MRI) and novel applications of wire metamaterials.

Georgiy Solomakha received the Ph.D. degree in antennas and microwave devices from the School of Physics and Engineering, ITMO University, Saint Petersburg, Russia, in 2021.

He is currently a Post-Doctoral Researcher with the School of Physics and Engineering, ITMO University. His current research interests include magnetic resonance imaging (MRI) coils for ultrahigh-field MRI.

Marc Dubois received the Ph.D. degree in condensed matter from Paris Diderot University, Paris, France, in 2014.

He is currently the Head of Research at Multiwave Imaging, Marseille, France. His current research interests include metamaterials and electromagnetism for magnetic resonance imaging (MRI) applications.

Redha Abdeddaim was born in Alger, Algeria, in 1979. He received the Ph.D. degree in physics from Paris X University, Paris, France, in 2007.

He is currently an Assistant Professor with Aix-Marseille University, Marseille, France. His current research interests include metamaterials, antennas, and magnetic resonance imaging (MRI) coils.

Stefan Enoch received the Ph.D. degree in 1997.

He is currently a Senior Researcher with CNRS, Paris, France, and the Deputy Vice President for Sciences and Technologies with Aix-Marseille University, Marseille, France. He has published about 150 research articles in top ranked journals and has given more than 40 invited and plenary presentations. His publications have been cited over 11 900 times and his H-index is 48. His research interests include the theory, modeling, and engineering of the interaction between waves and their environment. Though his main contributions are in optics and microwaves, he has also made significant contributions to mechanical waves in solids.

Dr. Enoch has been an Elected Fellow of the European Academy of Sciences in 2019 and a Fellow Member of the Optical Society of America in 2020. He received the Bronze Medal of CNRS in 2006 and the Aix-Marseille Innovation Award in 2019. He is a member of the Editorial Board of the *Journal of Modern Optics*. He was an Associate Editor of *Optics Express* from 2004 to 2012.

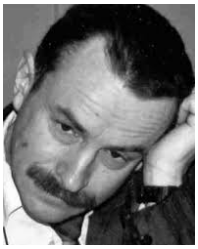

Constantin (Konstantin) R. Simovski received the Ph.D. and the Doctor of Sciences (Habilitation) degrees in physics and mathematics from St. Petersburg State Polytechnic University, Saint Petersburg, Russia, in 1986 and 2000, respectively.

From 1980 to 2001, he was with both industry and academic institutions in several countries. From 2001 to 2008, he was a Full Professor with ITMO University, Saint Petersburg. Since 2008, he has been with Aalto University, Espoo, Finland, where he has been a Full Professor since 2012. Since that time, the growth rate of his H-index has been constantly growing. His current research interests include metamaterials for optical sensing and energy harvesting, thermal radiation and radiative heat transfer, antennas for magnetic resonance imaging, wireless power transfer, and subwavelength optical imaging.

Stanislav Glybovski was born in Syktyvkar, Russia, in 1987. He received the M.Sc. and Ph.D. degrees in radiophysics from St. Petersburg Polytechnic State University, Saint Petersburg, Russia, in 2010 and 2013, respectively.

He is currently a Leading Researcher with the School of Physics and Engineering, ITMO University, Saint Petersburg. His current research interests include antennas and microwave devices, computational electromagnetics, metamaterials, and magnetic resonance imaging (MRI) coils.